

Finite Element Comparison of Homogenous Ridged and Non-Ridged X-Band Rectangular Waveguide Structures

Samuel J. Wyss[†]

[†]School of Nuclear Engineering
Purdue University
West Lafayette, Indiana 47907
E-mail: wysss@purdue.edu

Abstract—Two dimensional Finite Element Analysis (FEA) is applied to assess dispersion characteristics of homogenous rectangular, circular and ridged X-Band waveguide structures. To model these systems *in silico*, the weak form of the wave equation is derived from Maxwell's Equations for both TE and TM modes. Perfect electrical conductors (PECs) are used as waveguide walls as to neglect the effect of wave leakage into the environment. The model is validated against the analytical dispersion curves for rectangular and circular waveguides. A comparison of dispersion characteristics for ridged and non-ridged rectangular waveguides is provided which is then used to assess real world applications of ridged waveguides.

I. INTRODUCTION

Waveguides are used in a plethora of applications ranging from transmitting microwave fields to acting as passive low-pass filters [1]. While any cross section of a single conductor waveguide can support TE and TM modes, rectangular and circular cross sections are commonly chosen due to their ease of construction and analytic propagation characteristics. However, a limitation of rectangular waveguides is the limited bandwidth of their dominant mode which is less than an octave [1]. By adding a single or double ridge to the mouth of a waveguide, the cutoff frequency of the dominant mode can be reduced thus allowing for increased signal bandwidth [1]. This increased bandwidth comes at the cost of reduced power capacity due to the reduction in breakdown potential between the ridges [1] making them less ideal for High Power Microwave (HPM) devices.

All wave phenomenon in an arbitrarily shaped, infinitely long waveguide at a given frequency are governed by the frequency domain Maxwell's Equations. Of these equations, Faraday's and Ampère's laws, can be manipulated to create a vector Helmholtz wave equation which captures nearly all electromagnetic wave phenomenon to a high degree of accuracy [2]. The Finite Element Method (FEM) approaches the analytic solution of the wave equation by approximating a weak form of the equation over a finite set of elements within the simulation domain using weighted residuals. To convert the full wave equation to its weak form, the Galerkin method is employed for which the weighting functions are identical to continuous basis functions as is common in Computational Electromagnetics (CEM) Finite Element Analysis (FEA) [2].

In the case of an arbitrarily shaped, infinitely long waveguide, the full field, frequency domain solutions can be obtained by solving for the fields in a cross sectional slice of the waveguide. FEM operates on non-uniform, conformal meshes which allows for arbitrary waveguide cross sections to be modeled without stairstepping error unlike that of the structured meshes of Finite-Difference Time-Domain (FDTD). In addition to this, FEM allows for full three dimensional solutions of such a waveguide to be obtained by only solving for a representative two dimensional slice making FEM an ideal choice for this application.

The development and implementation of this work is laid out as follows. II contains the derivation of the vector Helmholtz equation from Maxwell's Equations using Galerkin's Method.

II. MATHEMATICAL MODEL

To model these systems *in silico*,

1) *Governing Equations*: The frequency domain Maxwell's Equations in the absence of electric or fictitious magnetic currents are,

$$\nabla \times \mathbf{E} = -j\omega\mathbf{B}, \quad (1)$$

and

$$\nabla \times \mathbf{H} = -j\omega\mathbf{D} \quad (2)$$

where \mathbf{E} is the electric field intensity, \mathbf{B} is the magnetic flux density, \mathbf{H} is the magnetic field intensity, and \mathbf{D} is the electric flux density.

For a homogenous, infinite waveguide filled with a non-dispersive dielectric, \mathbf{B} and \mathbf{D} can be rewritten as

$$\mathbf{B} = \mu\mathbf{H}, \quad (3)$$

and

$$\mathbf{D} = \epsilon\mathbf{E}. \quad (4)$$

These constitutive relations can now be used to simplify (1-2) as in

$$\nabla \times \mathbf{E} = -j\omega\mu\mathbf{H}, \quad (5)$$

and

$$\nabla \times \mathbf{H} = -j\omega\epsilon\mathbf{E}. \quad (6)$$

In the case of the infinite waveguide, the TM and TE modes can be fully solving for E_z and H_z respectively as all other field components can be derived from these two transverse fields [2]- [3]. With this, (5-6) can be manipulated to solve for two independent 2-dimensional Helmholtz equations as

$$\nabla_t^2 E_z + k_c^2 E_z = 0 \quad \text{on } \Omega, \quad (7)$$

and

$$\nabla_t^2 H_z + k_c^2 H_z = 0 \quad \text{on } \Omega \quad (8)$$

where $\nabla_t^2 = \partial_x^2 + \partial_y^2$ the the trasverse Laplacian operator in cartesian coordinates, $k_c^2 = \omega^2\mu\epsilon + k_z^2$ is the cutoff wave number, k_z is the wavenumber in the direction of propagation, and Ω denotes all non-boundary locations within the simulation domain.

These relations hold for all locations excluding those on the PEC walls of the waveguide. This PEC wall condition manifests in the form of a Dirichlet boundary condition

$$E_z = 0 \quad \text{on } \partial\Omega \quad (9)$$

for the TM mode and Neumann boundary conditions

$$\partial_x H_z = 0, \quad \partial_y H_z = 0 \quad \text{on } \partial\Omega \quad (10)$$

for the TE mode where $\partial\Omega$ denotes the PEC surface surrounding the waveguide.

2) *Galerkin Weak Formulation:* With the governing equations established, we can now proceed with the discretization of an arbitrarily shaped waveguide to solve for both the transverse electric and magnetic fields. Using FEM, we break these 2D waveguide slices into a finite set of finitely sized elements and approximate the solution of (7-8) over each element. Triangular elements are chosen as they can be meshed together to form the boundaries of arbitrarily curved shapes well making them ideal for modeling geometries with no analytic solutions [3]. Linearly interpolating functions are used to approximate the solution of (7-8) at the nodes of each element. Linear interpolating functions are chosen for their overall simplicity and adequate accuracy for the determination of waveguide parameters [2] [3].

For an arbitrary triangular element, an generic scalar field ϕ can be Linearly interpolated over using

$$\phi^{(e)}(x, y) = a + bx + cy \quad (11)$$

where (e) refers to a specific element, a, b, c are scaling constants and x, y are the coordinates of the location within the node [3]. This interpolation scheme can now be applied to find the field value at an arbitrary vertex on the element as

$$\phi_l^{(e)} = a + bx_l + cy_l \quad (12)$$

where x, y are the coordinates of the node [3]. These nodal field expressions can now be combined to rewrite (11) in terms

of the field value calculated at each node as

$$\begin{aligned} \phi^{(e)}(x, y) = & N_1^{(e)}(x, y)\phi_1^{(e)} \\ & + N_2^{(e)}(x, y)\phi_2^{(e)} + N_3^{(e)}(x, y)\phi_3^{(e)} \end{aligned} \quad (13)$$

with an arbitrary interpolating function $N_l^{(e)}$ given by

$$N_l^{(e)}(x, y) = \frac{1}{2\Delta^{(e)}} \left(a_l^{(e)} + b_l^{(e)}x + c_l^{(e)}y \right) \quad (14)$$

where $\Delta^{(e)}$ is the area of element e and $a_l^{(e)}, b_l^{(e)}, c_l^{(e)}$ are given by the following as in [3]

$$\begin{aligned} a_1^e &= x_2^e y_3^e - x_3^e y_2^e, b_1^e = y_2^e - y_3^e, c_1^e = x_3^e - x_2^e \\ a_2^e &= x_3^e y_1^e - x_1^e y_3^e, b_2^e = y_3^e - y_1^e, c_2^e = x_1^e - x_3^e \\ a_3^e &= x_1^e y_2^e - x_2^e y_1^e, b_3^e = y_1^e - y_2^e, c_3^e = x_2^e - x_1^e. \end{aligned} \quad (15)$$

With definitions (13-15) an arbitrary field with potential Dirichlet boundary conditions (noted by D) can be expressed as the superposition of all fields at each node as

$$\phi = \sum_{j=1}^N N_j \phi_j \sum_{j=1}^N N_j^D \phi_j^D \quad (16)$$

With the discretization of a generic field outlined, The Galerkin weak forms of (7-8) will now be derived in parallel. We begin by multiplying (7-8) by a weighting function which is identical to that of an interpolating function for the Galerkin procedure. The resulting weak forms are

3) Finite Element Matrix Assembly:

III. NUMERICAL RESULTS

All update equations as defined in Section ?? were implemented in Rust. This language was chosen for its C++ like performance while enforcing compile-time memory safety which makes writing fast and safe CEM codes relatively easy. An overview of this implementation can be found in V-A.

A. Verification and Validation

To verify and validate model results, the case of an infinitely long waveguide with fields propagating in the TE_{10} mode. This case is chosen as simulated results can easily be compared to analytic results.

All verification and validation analyses are performed with 0.1m stretch of a WR-90, X-band waveguide with a free space-filled, cross section of $a = 0.02286\text{m}$ and $b = 0.01016\text{m}$ [4]. Said configuration has an analytic TE_{10} cutoff frequency of as calculated by

$$f_c = \frac{c}{2\pi\sqrt{\epsilon_r\mu_r}} \sqrt{\left[\frac{m\pi}{a}\right]^2} \quad (17)$$

from [1]. Using free space dielectric parameters, this geometry has a cutoff frequency of 6.557GHz for the TE_{10} mode.

To ensure waves above the cutoff frequency are able to freely propagate, a monochromatic source as defined by (??) is used with a 10GHz carrier frequency with a ramp time of 5ns is used as an E_y driver function. The simulation was carried out using a time step of $\Delta t = 1.863\text{ps}$ over a 25ns duration

with spatial steps as $\Delta x = 0.994\text{mm}$, $\Delta y = 0.923\text{mm}$, and $\Delta z = 0.990\text{mm}$.

A spatial field profile of this system can be found in Fig. 1 along the y and x centerline planes.

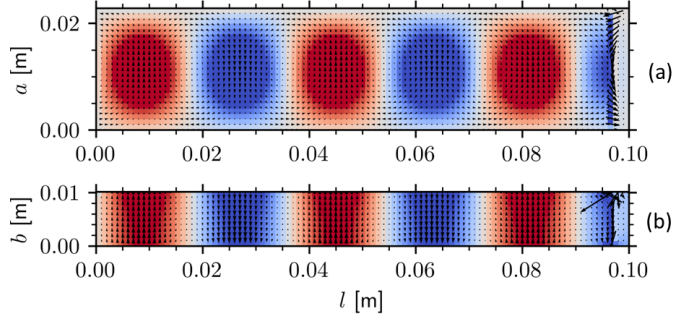


Fig. 1: Source Profiles at $t = 8.191\text{ns}$ for (a) E_y intensity (colored) with H_x, H_y directions (arrows) along the $y = 5.538\text{mm}$ plane and (b) H_x intensity (colored) with E_y, E_z directions (arrows) along the $x = 11.926\text{mm}$ plane

Arrows in Fig. 1 were scaled as to best show direction where as intensity colors were based off of the E_y sinusoidal amplitude. Colors for Fig. 1 (b) are scaled down by E_y/η_{10} as in (??). Field intensity was not explicitly labeled in Fig. 1 as it cluttered the plots and is not relevant for this analysis.

From visual inspection, it is quite clear that these field profiles match the theoretical frequency domain profiles as given in (??-??). Additionally, the validity of the TF/SF source and Mur's ABC is apparent from the relatively small fields found in the upper right of Fig. 1 (a) and (b). The small discrepancy in the upper right corner of 1 (b) is explained by leakage of the TF/SF source interacting with the PEC corner; both of which are liable for discrepancies as mentioned in [2].

To ensure the integrity of the wave propagating along the length of the waveguide, frequency spectra are taken of the source total field and transmitted total E_y field as found in Fig. 2. These transmitted and source spectra were taken at two representative voxels at $z = 4.950\text{mm}$ and $z = 95.050\text{mm}$ along the same x and y centerlines of Fig. 1. This choice of a centerline is arbitrary; changes in the x position would decrease the relative field intensity due to the sinusoidal profile necessitated by the PEC walls. Data for this plot was obtained by taking a field 'snapshot' 2,000 times over a the span of the 25ns simulation window with intermediate time spacing between samples of 13.043ps.

Fig. 2 clearly shows that all frequencies above the 6.557GHz cutoff frequency are able to travel along the length of the waveguide with minimal loss. These signals only differ for frequencies below that of the cutoff frequency of which fields are not able to propagate indefinitely.

With frequencies above the cutoff frequency able to freely propagate in the waveguide, it is now important to assess the waveguides performance in attenuating waves below the cutoff frequency. To test this property of our simulated waveguide, a wide-band modulated gaussian pulse as in (??) is used as a driver signal with a carrier frequency of 10GHz, ramp time of 0.5ns and delay time of 3ns. Frequency spectra at identical

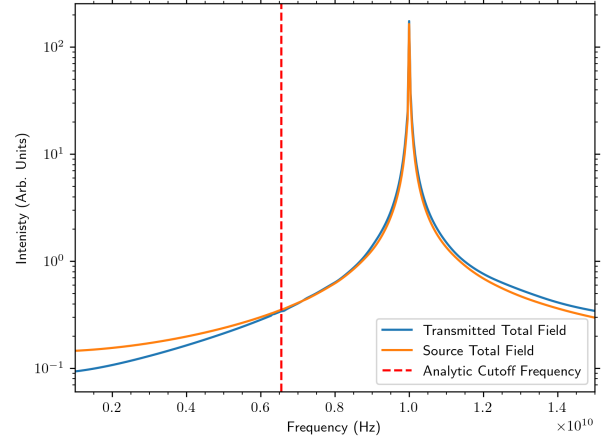


Fig. 2: Transmitted and Source Frequency Spectra with Labeled Cutoff Frequency for 10GHz Monochromatic Tapered Sine E_y Source

locations to that of Fig. 2 can be found below in Fig. 3. To facilitate the additional frequency content of the modulated Gaussian, field snapshots were taken at all 13,417 time steps over the simulation's 25ns duration.

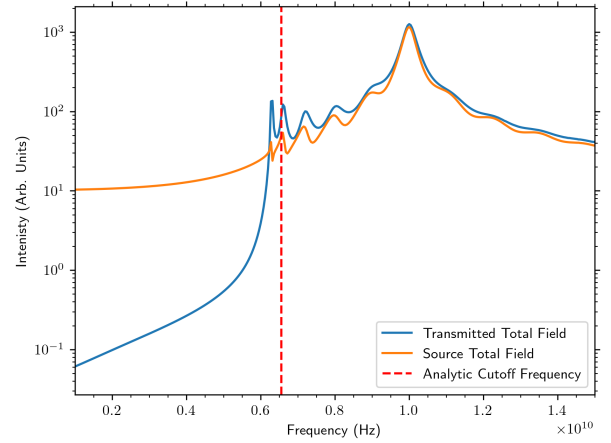


Fig. 3: Transmitted and Source Frequency Spectra with Labeled Cutoff Frequency for 10GHz Center Frequency, 0.5ns Ramp Time, Modulated Gaussian Pulse

As shown above in Figure 3 the *in silico* waveguide exhibits a cutoff frequency of approximately 6.2GHz which only differs from the theoretical by 5.444% making this model relatively realistic. Below this cutoff frequency, Fig. 3 shows a nearly two order of magnitude reduction in the transmitted while having little overall impact on frequencies above this which is expected.

B. Analysis of Unloaded Quality Factor with Varying Dielectric Loss

With the waveguide now successfully validated, the resonator performance can now be assessed using different di-

electric materials. More specifically, we aim to compare the performance of a cavity resonator filled with beeswax to that filled with beryllia at a frequency of 10GHz. Material properties for these materials are obtained from [1] which are used to derive conductivities for these materials at 25°C. For simplicity, the resonator cavity length is reduced from 0.1m to 0.05m to reduce the computational domain. An identical wideband carrier signal to that found in Fig 3 is used to look for resonances in these materials at and around 10GHz. For these simulations, the centermost E_y voxel is used as a representative sample of the whole domain. Due to these materials differing relative permittivities, the centermost voxel may exist at slightly different physical locations within the simulation; however, this discrepancy is assumed to be small. results for this comparative study can be found below in Fig. 4.

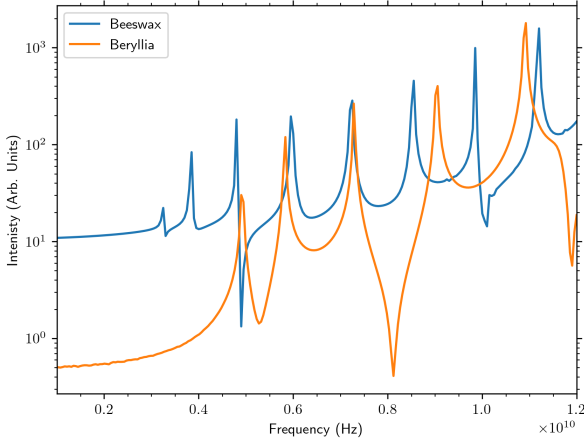


Fig. 4: Centermost Voxel Frequency Spectra for Beeswax and Beryllia for 10GHz Center Frequency, 0.5ns Ramp Time, Modulated Gaussian Pulse

These two materials exhibit far more complex interactions than that of free space with numerous resonances exited in both materials. With its lower loss tangent of $\tan \delta = 0.0003$ and higher unloaded dielectric quality factor $Q = 3333.3$, beryllia resonates several times more than beeswax with a loss tangent of $\tan \delta = 0.005$ and $Q = 200$ at 10GHz. Interestingly the beeswax-filled cavity resonator exhibits more peaks than that of beryllia over the 1 – 12GHz domain. This is likely a direct result of the complex interaction between resonator shape, dielectric properties, and wavelength as described in [1].

IV. CONCLUSION

A 3-dimensional finite difference time domain was developed from Maxwell’s Equations for a rectangular waveguide and cavity resonator. The model was validated against analytic results for narrow and wide band signals thereby verifying

the model’s calculated fields. From this, several dielectric materials were compared for use in X-Band cavity resonators at 10GHz. These compared results were then explained using theoretical unloaded quality factors further verifying the accuracy of the model.

While relatively performant, there are many optimizations that could be made to the underlying implementation. Most notably tiled approaches could be taken to improve program cache locality to alleviate the memory bound nature of the loops in this implementation. Tiled approaches would also aid in exploiting the embarrassingly parallel structure Yee’s FDTD algorithm gives rise to. Further improvements could also be made to the implementation to allowing for more complex geometries to be represented which may be useful for placing devices inside waveguides or using the waveguide as a source for another device. Finally, the user experience of this implementation should be improved as it is remarkably easy to save in tens to hundreds of gigabytes of data inadvertently shifting the bottleneck away from memory to disk performance.

V. APPENDIX

A. Code Structure

Code is broken up into logical modules, as is custom in Rust, which contain related aspects of the code. The file `./src/main.rs` contains the ‘main’ function that is built into a binary. The file `./src/solver.rs` contains a high level interface for interacting with and bootstrapping the simulation. The file `./src/geometry.rs` contains a structure that holds information relevant to the geometry of the simulation. Finally, the `./src/engine.rs` contains all data and methods needed to evolve the simulation in time and contains much of the simulation code. All functions are commented using function comments in the source code which are automatically assembled into an interactive webpage containing all project documentation. Said documentation can be found under the `./doc/` directory. As such project documentation can either be viewed by looking at the source code and/or viewing the interactive documentation pages by opening `./doc/waveguide/index.html` with a web browser. The code can easily be compiled with cargo (the package manager that comes with Rust much like Pip for Python) using the command `cargo build --release`. The compiled binary can then be executed by running `./target/release/driver.exe`. This binary reads in data from `config.toml` which contains all simulation parameters.

REFERENCES

- [1] D. M. Pozar, *Microwave Engineering*. John Wiley & Sons, 2011.
- [2] T. E. Roth, *ECE 61800 Lecture Notes*. Purdue University, 2024.
- [3] J.-M. Jin, *Theory and Computation of Electromagnetic Fields*. John Wiley & Sons, 2011.
- [4] Everything RF contributors, “Rectangular waveguide sizes,” <https://www.everythingrf.com/tech-resources/waveguides-sizes>, 2021, [Online; accessed 28-February-2024].